Cement & Concrete Composites 38 (2013) 82–91

Contents lists available at SciVerse ScienceDirect

Cement & Concrete Composites

journal homepage: www.elsevier.com/locate/cemconcomp

Physical and mechanical characterization of Fiber-Reinforced Aerated Concrete (FRAC)

A. Bonakdar [a,*], F. Babbitt [b], B. Mobasher [a]

[a] School of Sustainable Engineering and the Built Environment, Arizona State University, Tempe, AZ, USA
[b] Babbitt Nelson Engineering, LLC, Mesa, AZ, USA

ARTICLE INFO

Article history:
Received 15 March 2012
Received in revised form 16 February 2013
Accepted 17 March 2013
Available online 27 March 2013

Keywords:
Aerated concrete
Fiber-reinforced concrete
Mechanical properties
Pore-structure
Sustainability
Thermal conductivity
Toughness

ABSTRACT

Fiber-Reinforced Aerated Concrete (FRAC) is a novel lightweight aerated concrete that includes internal reinforcement with short polymeric fibers. The autoclaving process is eliminated from the production of FRAC and curing is performed at room temperature. Several instrumented experiments were performed to characterize FRAC blocks for their physical and mechanical properties. This work includes the study of pore-structure at micro-scale and macro-scale; the variations of density and compressive strength within a block; compressive, flexural and tensile properties; impact resistance; and thermal conductivity. Furthermore, the effect of fiber content on the mechanical characteristics of FRAC was studied at three volume fractions and compared to plain Autoclaved Aerated Concrete (AAC). The instrumented experimental results for the highest fiber content FRAC indicated compressive strength of approximately 3 MPa, flexural strength of 0.56 MPa, flexural toughness of more than 25 N m, and thermal conductivity of 0.15 W/K m.

1. Introduction

Physical and mechanical characteristics of Fiber-Reinforced Aerated Concrete (FRAC) were studied in this work. Several instrumented experiments were performed to characterize FRAC and Autoclaved Aerated Concrete (AAC) blocks. These studies include the measurement of pore-structure; the variations of density and compressive strength within a typical block; compressive, flexural and tensile properties; impact resistance; and thermal conductivity. The effect of fiber content on the mechanical properties of FRAC was studied at three volume fractions and compared to AAC.

1.1. Aerated Concrete and sustainability

The worldwide cement production results in approximately 5% of global manmade carbon dioxide emissions [1]. From a life-cycle perspective, however, the energy consumption and the resulting CO_2 emission from the operation of buildings are much larger than the energy consumed during production of the building materials. In essence, only 3% of the total energy consumed in a typical building is attributed to the production of the building materials used in the construction [2] and the rest is consumed during the service life of the building. This indicates that developing efficient construction products can be a cost effective way to reduce our overall energy consumption. Aerated concrete is a class of construction materials which can serve the purpose of manufacturing and construction efficiency and thermally attractive products.

Aerated Concrete (AC) is a lightweight, noncombustible cement-based material, manufactured from a mixture of Portland cement, fly ash (or other sources of silica), quick lime, gypsum, water, and aluminum powder (or paste) as described in ACI 523.2R [3]. Aerated concrete products are traditionally autoclaved for accelerated strength gain; hence they are commonly referred to as Autoclaved Aerated Concrete (AAC). The air-pores in aerated concrete are usually in the range of 0.1–1 mm in diameter and typically formed by the addition of aluminum powder (or paste) at 0.2–0.5% (by weight of cement). The chemical reaction of calcium hydroxide and aluminum generates hydrogen gas shown in Eq. (1) is associated with large volume changes, resulting in the expansion of the fresh mixture to about twice of its original volume. Narayanan [4] reported that approximately 80% of the volume of the hardened material is made up of pores with a general ratio of 2.5:1.0 air-pores to micro-pores.

$$2Al + 3Ca(OH)_2 + 6H_2O \rightarrow 3CaO \cdot Al_2O_3 \cdot 6H_2O + 3H_2 \uparrow \quad (1)$$

In order to further focus on sustainability, supplementary cementitious materials such as slag, fly ash and silica fume have been increasingly used to improve aerated concrete. One example of this trend is the movement towards high volume fly ash (HVFA)

* Corresponding author. Tel.: +1 480 246 0917; fax: +1 480 965 0557.
E-mail address: amirb@asu.edu (A. Bonakdar).

0958-9465/$ - see front matter © 2013 Elsevier Ltd. All rights reserved.
http://dx.doi.org/10.1016/j.cemconcomp.2013.03.006

concretes, where up to 50% or more of the cement is replaced with fly ash (Mehta [5] and Bentz et al. [6]). The utilization of high volume fly ash in the production of aerated concrete contributes to additional benefits in the reuse and recycle of coal combustion by-products. It has been suggested that more than 400,000 tons of fly ash can be used in aerated concrete blocks in the future [7]. Partial replacement of cement with fly ash can also improve the durability of concrete products in exposure to external sulfate attack and alkali–silica reaction (Bonakdar and Mobasher [8] and Bonakdar et al. [9]).

The main characteristic of aerated concrete is the high porosity, resulting in lower density and compressive strength compared to normal-weight concrete. ASTM C-1693 (previously C-1386) classifies aerated concrete based on the dry density of 400–800 kg/m^3 and compressive strength values of 2–6 MPa [10]. The pore structure consists of a variety of sizes from micro-pores to macro-pores and air-pores [11] and results in excellent thermal properties. Comparative evaluation of the embodied energy data indicates that AC is a viable alternative to similar construction materials such as concrete or brick with as much as 70% and 40% energy reduction, respectively, per volume of material [12]. Several studies have been performed on the thermal properties of aerated concrete as a function of its density. It was shown by Narayanan [7] that thermal conductivity of AC with dry density of 400 kg/m^3 was 0.07–0.11 W/m °C which is about 10–20 times less than normal-weight concrete (which is in the range of 1.6–1.8 W/m °C). A recent study performed by Ng and low [13] on denser aerated concrete showed conductivity values to be approximately 0.39, 0.50, and 0.62 W/m °C for unit weights of 1100, 1400, and 1700 kg/m^3, indicating a linear trend. The pore structure of AC also affects the acoustic properties and sound transmission, making it a good sound insulator [14]. The mechanical properties of AAC including compressive strength, flexural strength, and fracture energy as reported in the literature [15,16] indicate a linear relationship with density in the range of 600–1200 kg/m^3.

1.2. Fiber-Reinforced Aerated Concrete

A novel class of aerated concrete is Fiber-Reinforced Aerated Concrete (FRAC) or FlexCrete® which includes internal reinforcement with short polymeric fibers such as polypropylene. In order to avoid potential damage to the polymeric fibers, autoclaving is eliminated from the production of FRAC and curing is performed at room temperature. Elimination of autoclaving process may create lower strength values and higher inhomogeneity when compared with autoclaved aerated concrete. The structures of FRAC and AAC are therefore of different natures. Short fibers however have a positive effect in bridging the cracks formed during the plastic stage or later on due to the mechanical forces, drying shrinkage, or heating–cooling cycles. It has been reported by Perez-Pena and Mobasher [17] that the addition of short polypropylene fibers to lightweight cementitious panels can largely improve the mechanical properties. In their study, modulus of rupture increased from 3.2 to 4.0 MPa and toughness increased from 0.6 to 1.2 N m when fiber content was raised from 0.4% to 1.4%. Additionally, adding short fibers reduces the shrinkage cracking in the plastic phase or later in the elastic phase while drying [18].

Aerated concrete products can exhibit a considerable amount of residual compressive strength after reaching the peak strength [19]. As shown in Fig. 1a for compression behavior of these materials and after the initial linear response, pore crushing stage starts, showing an uneven plateau region. The load-carrying mechanism after the peak load can be attributed to sequential pore crushing and collapse of the cell walls under compressive pressure. Assuming that these responses are consistently obtained, one can utilize them for nonlinear approaches for analysis and design. From an ultimate strength point of view, the performance can be modeled using an elastic–plastic response that uses the post cracking residual strength of the cellular material. The ratio of residual strength to peak strength for FRAC is typically more than AAC due to the role of fibers in integrating the structure. Fig. 1b shows the tensile/flexural behavior of these cellular solids. AAC shows a brittle failure once the ultimate strength is reached, however, FRAC shows a ductile response due to the role of short fibers in bridging the tensile cracks. The economical approach for studying and utilizing FRAC is based on the similarities of this material to Autoclaved Aerated Concrete (AAC) and Fiber-Reinforced Concrete (FRC).

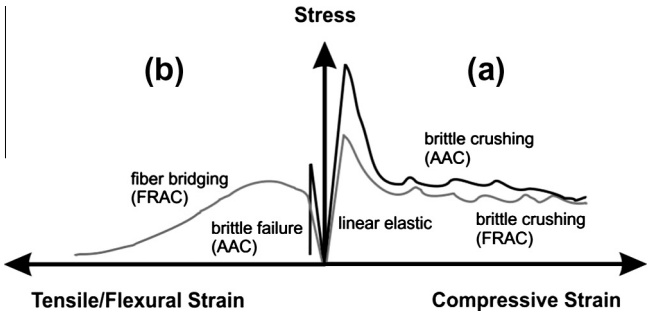

Fig. 1. Schematic presentation of stress–strain response for AAC (black) and FRAC (gray).

2. Experimental procedure

The ingredients of the studied FRAC include portland cement, fly ash, water, aluminum paste, polypropylene fibers and chemical admixtures as presented in Table 1. The mixture proportions for the studied AAC are also presented in this table. It should be noted that due to the autoclaving process, the microstructure of hardened AAC is different than of FRAC. These materials are weighted and mixed using an automated batching system. The water used for mixing is preheated to about 38 °C to accelerate the reaction, which in turn generates more heat through exothermic reactions within the first 24 h. The fresh mixture is poured into large 8 m × 1.2 m steel molds with a depth of 0.6 m. The dimensions of these steel molds depend on the desired size of final products, the size of manufacturing plants, and also the capacity of machineries. Since FRAC is manufactured without reliance on the autoclave process, the temperature distribution throughout the solid mass is affected by the interaction of the size of the samples with internal heat generation, the ambient curing environment, and the thermal history. The temperature rises as much as 30° during the initial hours due to the chemical reactions which may generate micro-cracks in the material. These mechanisms introduce

Table 1
Mix proportions for AAC and FRAC (weight %).

Material	FRAC-A	FRAC-B	FRAC-C	AAC
Cement	28	28	28	18
Fly ash	42	42	42	0
Silica	0	0	0	27
Lime stone + gypsum	0	0	0	8
Recycled material	0	0	0	9
Water ~38 °C (100°F)	28	28	28	38
Fiber (polypropylene)	0.4	0.3	0.2	0
Aluminum paste	<0.1	<0.1	<0.1	<0.1
Other additives (classified)	0.3	0.3	0.3	0

Note: FRAC is cured at room temperature, however AAC is autoclaved for accelerated curing.

additional inhomogeneity and consequently more variability in the test data.

Experiments were conducted in order to characterize FRAC with varying amounts of fiber reinforcement (with same densities) for their physical and mechanical properties. The objective was to correlate the mechanical properties with the level of fiber reinforcement and characterize the overall performance of the material given the degree of variation that exists due to pore volume. The studies included determination of pore-structure at micro-scale and macro-scale; variations of density and compressive strength in the blocks; compressive stress–strain properties (strength, modulus of elasticity and Poisson's ratio); flexural and tensile stress-cracking; crack–width relationship properties; impact test using instrumented hammer drop; and thermal conductivity. Mechanical tests were performed using computer-controlled servo-hydraulic machines under closed-loop condition. Three volume fractions of polypropylene fibers were used and the corresponding mixtures were labeled as FRAC-A ($V_f = 0.36\%$), FRAC-B ($V_f = 0.27\%$) and FRAC-C ($V_f = 0.18\%$).

3. Results and discussion

3.1. Thermal properties

A modified version of ASTM C-177 [20] was used for measuring the thermal conductivity of FRAC using guarded hot plate procedure. The experiment was performed similarly to the works done by Ng and Low [15] and Othuman [21]. As shown in Fig. 2, two 300 mm × 300 mm × 20 mm (12″ × 12″ × 0.8″) plates were tested simultaneously with six thermocouples for each sample: three on the top surface and three on the bottom surface. Temperature data were collected using a data acquisition system and the values of thermal conductivity were measured for AAC and FRAC-A. The test runs until reaching a steady-state for which thermal conductivity can be calculated as shown in Fig. 3 for FRAC-A. This procedure applies a one-dimensional heat flow q_x through a specimen of a cross section A, to produce a temperature gradient across the thickness dT/dx. This allows for the thermal conductivity k of the material to be determined (in W/m K) using the Fourier's Law shown in Eq. (2). More details to this heat transfer problem are explained by the authors elsewhere [22].

$$q = -k \cdot A \cdot \frac{dT}{dx} \tag{2}$$

Four replicate samples were used for each mixture. Thermal conductivity (k) is a function of moisture condition, i.e. the higher the moisture content, the larger the conductivity coefficients [23]. Therefore it is important to consider the moisture content when testing for thermal properties and have drying procedures before the test. The values of thermal conductivity for AAC, FRAC-A, and dried FRAC-A were measured experimentally and the results are summarized in Table 2. The AAC material showed less scattered results with an average k of 0.176 ± 0.001 W/K m (1.218 ± 0.007 Btu in./h ft^2 °F) while FRAC-A showed less uniformity with an average K of 0.215 ± 0.028 W/K m (1.490 ± 0.195 Btu in./h ft^2 °–F) in non-dried state and 0.150 ± 0.016 W/K m (1.043 ± 0.112 Btu in./h ft^2 °F) in the dried condition. These values are as much as 10 times less than normal-weight concrete, implying good insulation properties for FRAC material, especially in dry condition. The accuracy of the test method was examined by testing calibration materials with known conductivity values. Plexiglas and cement-board were tested and the obtained thermal conductivity values were 0.188 W/m K and 0.335 W/m K, respectively, falling in the available reported conductivity ranges. Calculation of the effective thermal conductivity of porous materials from the conductivity of constituents and the porosity could be done by deriving the related heat transfer equations and developing finite-elements models [24,25].

3.2. Pore-structure

Pore-structure studies provided an estimate of the porosity and the distribution of the air-pores. Fig. 4 represents a scanning electron micrograph of the pore-structure of FRAC-A, showing both the air-pores (in the approximate range of 200 μm to 1 mm) and the fibers. The porosity is higher at the top region of the block due to the upward movement of hydrogen gas during the initial hours. The rheology of the fresh paste and the particle size of the aluminum paste and reactivity has therefore a profound effect on the nature of pore distribution throughout the vertical direction. Blocks of 200 mm × 200 mm × 600 mm (8″ × 8″ × 24″) in dimension were obtained from several loaves representing the direction of the rise in the sample. Each block could therefore be used to represent the gradual changes in the porosity and strength within each sample.

Image analysis was used for determining the variation of porosity in each block. Plates with dimensions of 200 mm × 200 mm × 10 mm (8″ × 8″ × 0.4″) were cut and used for studying the pore-structure. These plates were dusted off, washed, and dried prior to image analysis. A high resolution digital scanner was used for obtaining images with 600 dpi at each depth. These images were then split into 64 smaller of the size 25 mm × 25 mm (1″ × 1″) sub-images for individual analyses using segmentation approach similar to Stang et al. [26]. Fig. 5a shows a typical gray-scale image while Fig. 5b presents the converted black and white (binary) image. The ratio of black to white area is defined as the 2-D pore-ratio and was calculated for all the 64 images for each 200 mm × 200 mm (8″ × 8″) plate. The average values, representing the pore-ratio of each depth, were used for comparison of plates obtained at various depths.

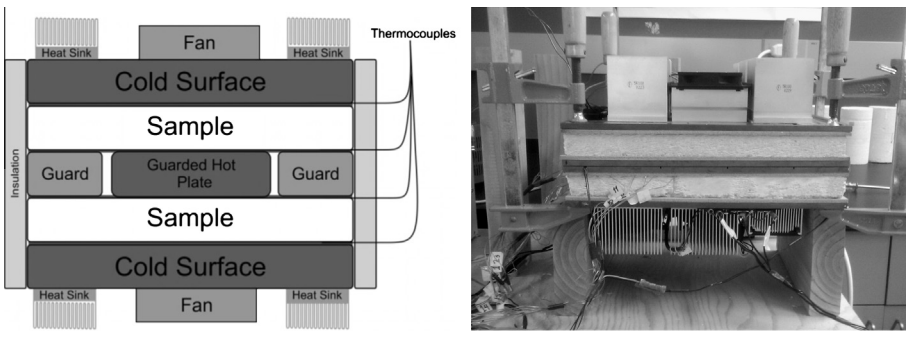

Fig. 2. Thermal conductivity (guarded plates) test setup (two 20 × 300 × 300 mm plates).

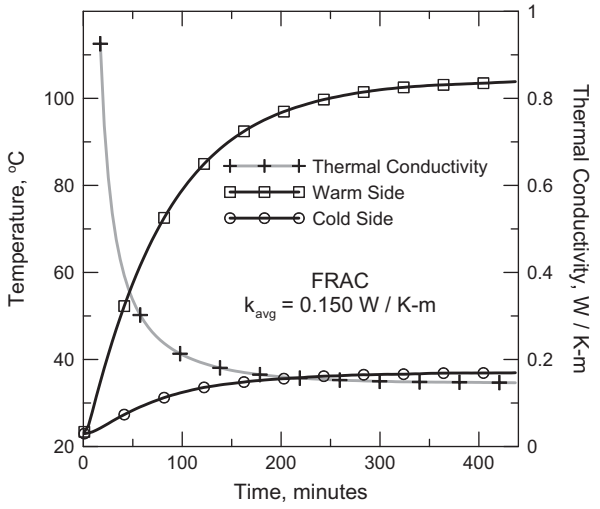

Fig. 3. Thermal conductivity measurement for FRAC-A (dried sample).

Table 2
Thermal conductivity values: W/°K m.

	FRAC	FRAC (dried)	AAC
Samples 1 and 2	0.195	0.139	0.175
Samples 3 and 4	0.235	0.162	0.177
Average	0.215	0.150	0.176

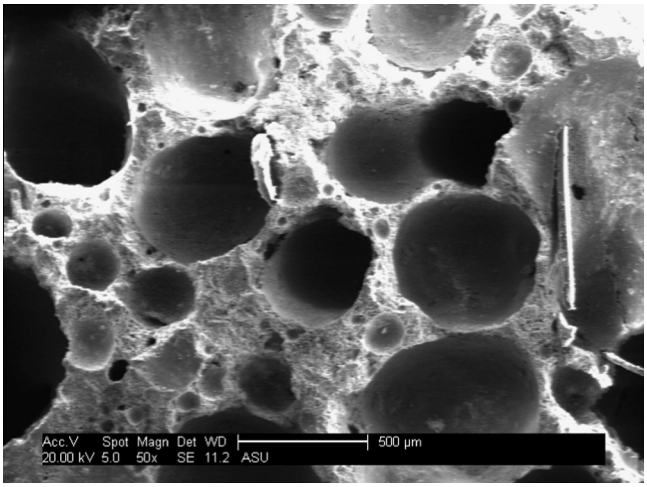

Fig. 4. Scanning electron micrograph of FRAC showing the pores and the fibers.

Seven plates were obtained at intermediate sections along the length of a typical block as shown in Fig. 6. The variations of the density and pore ratio in the longitudinal direction of a typical FRAC-A block are shown in Fig. 6a and b, respectively. The 2-D pore-ratio changed from about 0.3 at the bottom to about 0.5 at the top of the block, while the density changed from 620 kg/m^3 (39 lb/ft^3) to about 530 kg/m^3 (33 lb/ft^3). Pore ratio data are average values for 64 images for each plate while density data represent single measurement for each sample. This analysis is based on 2-dimensional images and the results present the 2-D observed porosity. A conversion of 2-D to 3-D porosity is however possible using stereological methods [27]. By measuring the diameter of 2-D pores and their distribution in a unit area, one can estimate the average diameter of 3-D pores as described in Eq. (3). In these equations, d is the diameter of individual 2-D pores; D' is the mean diameter of 3-D pores; N_A is the number of pores in 2-D in unit area; N_V is the number of pores in 3-D in unit volume and $H(d)$ is the Harmonic mean of diameters in 2-D.

$$D' = \frac{\pi}{2} \cdot H(d) \qquad N_V = \frac{N_A}{D'} \tag{3}$$

This analysis was performed on several randomly-selected images of 25 mm × 25 mm (1″ × 1″) size and the 2-D diameters of 20 pores were measured, followed by the calculation of 3-D diameters. Fig. 7 shows the distribution of 2-D and corresponding 3-D diameters for two sets of data obtained from the bottom and top of the block. As expected, the pore diameters are larger at the top (0.71 mm 2-D and 1.07 mm 3-D) in comparison with the bottom (0.52 mm 2-D and 0.72 mm 3-D) for this block. The gross total porosity can be calculated by having the bulk density (ρ_b) and the pure density (ρ_p) of FRAC following Eq. (4) [28]. In this case, the approximate values are 600 kg/m^3 and 2,600 kg/m^3 respectively, resulting in a total porosity of 77% for the studied FRAC block.

$$P = \left(1 - \frac{\rho_b}{\rho_p}\right) \times 100\% \tag{4}$$

3.3. Density and strength variations

The main properties of FRAC used for the classification and engineering application are the dry density and compressive strength, in accordance to ASTM C- 1693 [11]. This standard suggests testing three 100 mm (4″) cube samples obtained from three different depths of the block, named here as top (N7), middle (N4), and bottom (N1). The average density and compressive strength values are used for classification. Fig. 8 shows the compressive

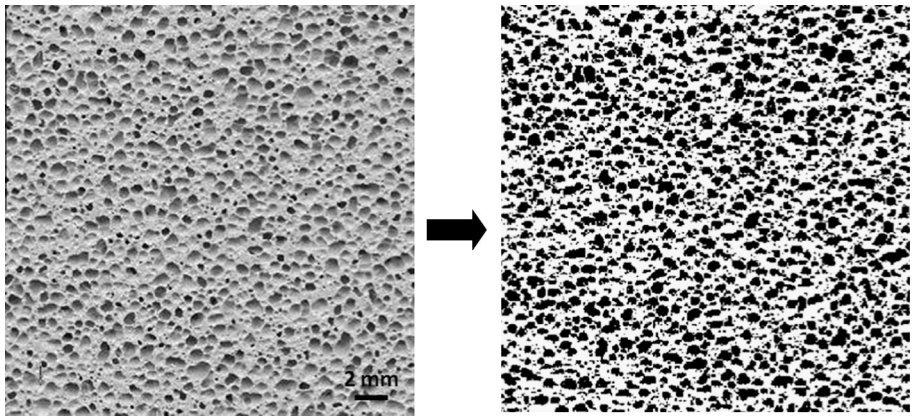

Fig. 5. Conversion of the gray-scale image to binary image.

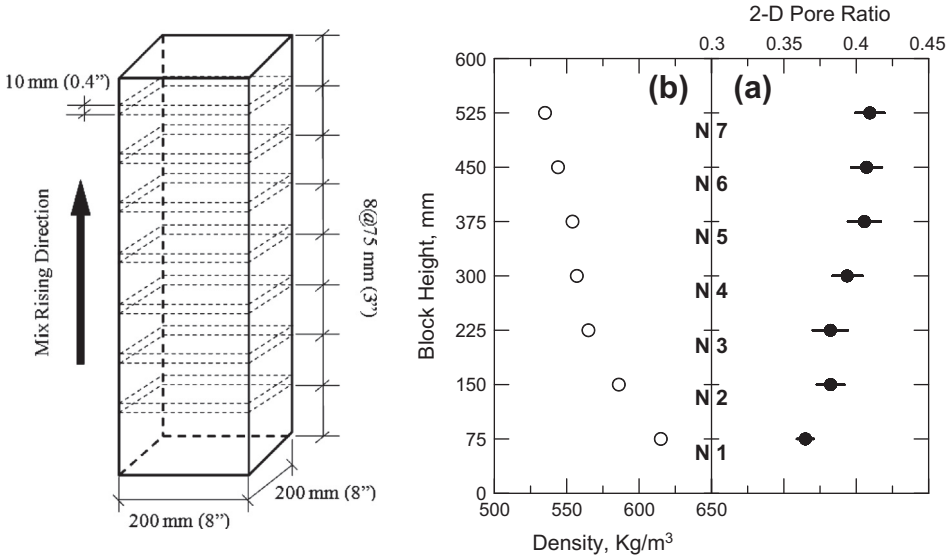

Fig. 6. Variations in the longitudinal direction of a block: (a) 2-D pore ratio, and (b) density.

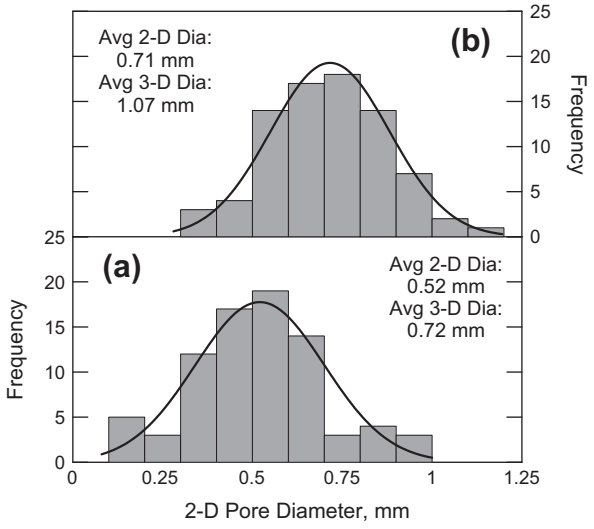

Fig. 7. Distribution of 2-D pore diameter: (a) for N7 (top), and (b) for N1 (bottom).

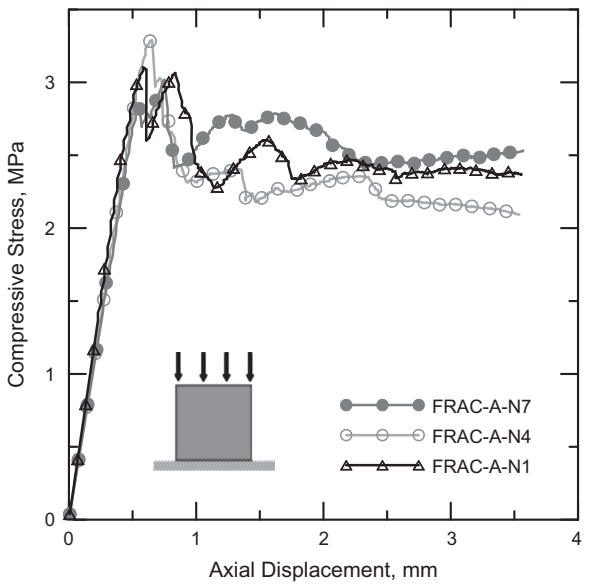

Fig. 8. Typical compressive behavior for FRAC-A using cubes. Note: N1, N4, N7 stand for the cubes obtained from the bottom, middle, and top portion of a typical block.

behavior of these three cubic samples for a typical FRAC-A block. One can see that the maximum strength is slightly different for these blocks (2.9, 3.1, 3.3 MPa) with a residual strength value of about 2.4 MPa.

More than 280 compression samples (FRAC-A) using $100 \times 100 \times 100$ mm ($4 \times 4 \times 4$ in.) cubes were tested and the histogram are presented in Fig. 9a and 9b. The value of (non-dried) density for tested samples was 658 ± 26.3 kg/m^3 (41 ± 1.6 lb/ft^3) and the compressive strength was 3.2 ± 0.73 MPa (646 ± 106 psi). Normality test was performed on the strength and density distribution and showed normal distribution for both density and strength with P-values < 0.005. The Anderson Darling (AD) values were 1.6 and 4.6 and the skewness factors were 0.21 and 0.57 for density and strength, respectively. Note that these results represent average values from samples obtained from random locations throughout the section. A linear relationship between density (or porosity) and compressive strength for aerated concrete has been reported by Narayanan [4] and Alexanderson [29]. The density and strength values for the studied FRAC material well match this linear trend.

3.4. Compressive stress–strain relationship

The test configuration needed for obtaining the stable post-peak compressive response depends on the behavioral class and the brittleness of the material. The general guidelines in ASTM C-469 [30] were followed for measuring the modulus of elasticity and Poisson's ratio. As shown in Fig. 10 and 75 mm × 150 mm ($3'' \times 6''$) cylinders (obtained by coring) were tested for instrumented compression using two LVDTs (for the axial displacements) and an extensometer (for the circumferential displacement). A servo-valve hydraulic system was used under closed-loop condition for performing these tests under crack-opening displacement (COD) control. Post-peak response can be obtained by an extensometer placed using a chain type fixture around the specimen to measure the circumferential displacement as the control. The values of the modulus of elasticity and Poisson's

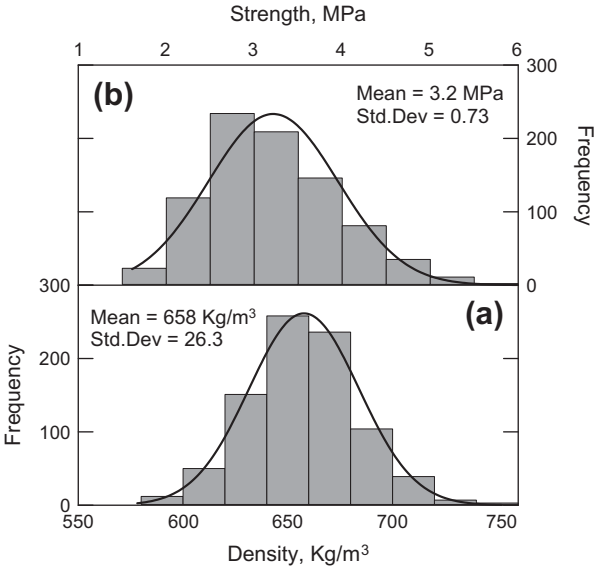

Fig. 9. Distribution of the field data: (a) density, and (b) strength for 861 cubes (FRAC-A).

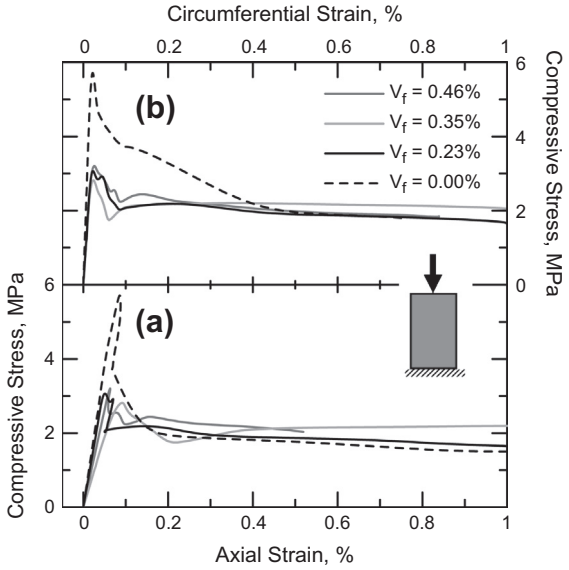

Fig. 11. Compressive strength vs. (a) axial strain, and (b) circumferential strain.

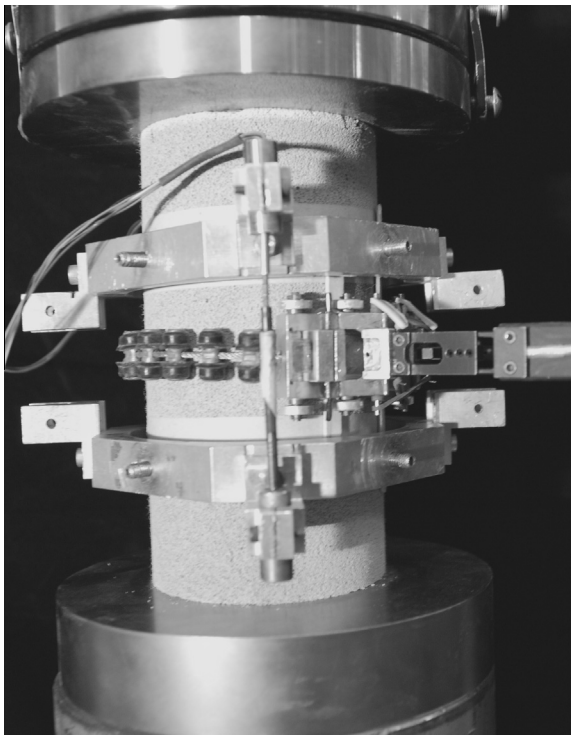

Fig. 10. Instrumented compression test setup (75 × 150 mm cylinder).

ratio were measured using the data for AAC, as well as FRAC with different volumes of fibers. Three replicate samples were used for each mixture.

Fig. 11 shows the instrumented compression test result for the measurement of stress–strain response for AAC and FRAC. Fig. 11a represents the stress vs. axial strain and Fig. 11b corresponds to the stress vs. circumferential strain. The linear portion of the curves (before cracking) was used for calculating the modulus of elasticity of the material and the ratio of the circumferential to axial strains was used for calculating the Poisson's ratio. The calculated values of compressive strength (F_c), modulus of elasticity (E), Poisson's ratio (v) and axial and circumferential stiffness (slopes of stress–strain curves in the linear portions) are summarized in Table 3. While AAC showed an F'_c of 5.6 MPa (814 psi), FRAC mixtures had F'_c in the range of 3.0–3.2 MPa (440–470 psi). For a proper comparison of the compressive strength values, one should note that AAC was autoclaved, however FRAC was cured at ambient temperature and it included 50% cement and 50% fly ash in its mix design.

The residual strength in the post-peak region was about 30% for AAC and about 60% for FRAC-A, implying the role of short fibers in keeping the integrity of material during cell crushing process. The residual strength was 1.52 MPa (220 psi) for AAC and 1.76 MPa (255 psi) for AAC FRAC-A. Compressive toughness was calculated using the area under the load–displacement curves (actuator data) as presented in this table for two strains levels of 1.3% and 1.5%. The value of Young's modulus for AAC was 7.5 GPa (1088 ksi) and for FRAC mixtures in the range of 4.5–5.0 GPa (650–730 ksi). The values of Poisson's ratio however, were more uniform for all the mixtures, ranging between 0.26 and 0.27.

3.5. Flexural load-deformation properties

Flexural testing of FRAC and AAC was performed on 150 mm × 150 mm × 500 mm (6″ × 6″ × 20″) beams with a span of 450 mm (18″) and a notch size of 25 mm (1″) using an instrumented three-point bending configuration, shown in Fig. 12. An LVDT was used for the axial displacement and a clip-gage was used for crack mouth opening displacement (CMOD); the test was performed under CMOD control with closed-loop condition for capturing the post-peak region. The values of the PEL stress, deviation from linearity, stiffness, modulus of rupture (MOR) and flexural toughness were measured using the data for AAC, as well as FRAC-A, FRAC-B, and FRAC-C. Three replicate samples were used for each mixture.

The results of the instrumented flexural test for AAC and FRAC are presented in Fig. 13 showing the flexural strength vs. axial displacement. AAC behaved in a brittle manner and failure occurs as soon as the peak strength was reached. There was virtually little or no resistance to propagation of tensile cracks and post-peak response was associated with unstable crack growth and total loss of load carrying capacity. The peak strength for FRAC was reached in the non-linear portion of the curve where strain-hardening was taking place. The post-peak response of FRAC is associated with

Table 3
Summary of compression test parameters for AAC and FRAC.

	FRAC-A	FRAC-B	FRAC-C	AAC
F_c: MPa	3.05	3.22	3.20	5.61
Residual strength: MPa	1.76	1.73	1.71	1.52
Residual strength ratio	0.58	0.54	0.53	0.27
Elastic modulus: GPa	5.02	4.95	4.51	7.50
Poisson's ratio	0.27	0.26	0.27	0.26
Toughness at 1.3% strain: N m	44.56	41.43	40.53	49.67
Normalized toughness at 1.3% strain level: N/m	9,902	9,206	9,005	11,037
Toughness at 1.5% strain: N m	64.07	62.39	57.92	64.64
Normalized toughness at 1.5% strain level: N/m	14,238	13,864	12,871	14,364
Axial displ. at peak: mm	0.036	0.031	0.037	0.044
Circm. displ. at peak: mm	0.085	0.062	0.067	0.062

Note 1: mix designs and curing methods are different for AAC and FRAC.
Note 2: toughness was measured by calculating the area under the compressive load–displacement curves, therefore, has unit of N m. Normalized compressive toughness was measured by dividing the toughness value by the cross sectional area with a resulting unit of: N/m.

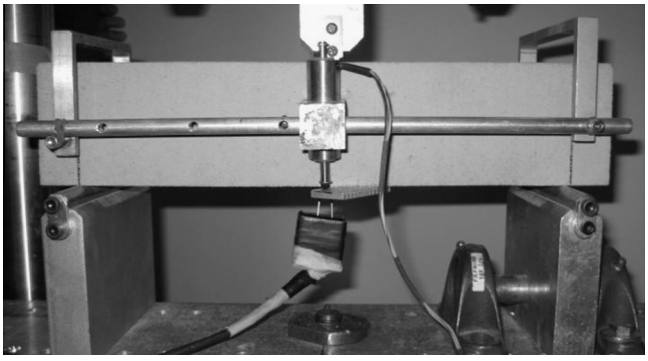

Fig. 12. Instrumented flexural test setup (150 × 150 × 450 mm notched beam).

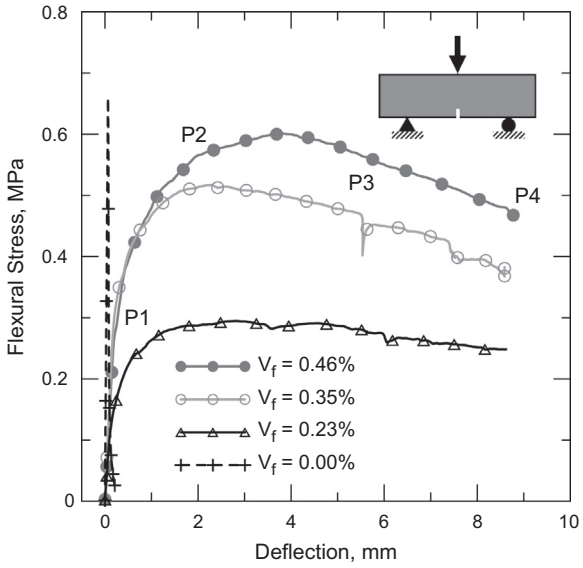

Fig. 13. Flexural strength vs. deflection for AAC and FRAC. Note that the images corresponding to P1–P4 are shown in Fig. 14.

large amount of energy dissipation and significant strain softening. Fig. 14 shows the bridging action of polypropylene fibers during the flexural loading for FRAC-A. Four points (P1, P2, P3, P4) correspond to the points shown in the previous figure. Experimental parameters of the flexural tests are summarized in Table 4 for AAC and FRAC beams. These include modulus of rupture (MOR), deflection at the maximum load, elastic flexural stiffness (slope of stress–displacement curve in the linear portion), and flexural

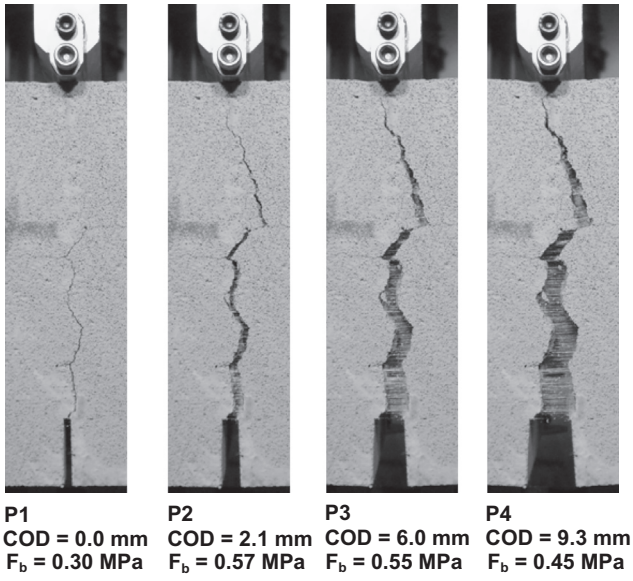

Fig. 14. Crack bridging for FRAC-A during flexural test corresponding to P1–P4.

toughness (using the displacement values from the actuator). The average value of MOR for AAC was 0.66 MPa (95 psi), while FRAC mixtures had MOR values of 0.56 MPa (81 ksi), 0.43 MPa (62 ksi), and 0.27 MPa (39 ksi) for FRAC-A, FRAC-B, and FRAC-C, respectively. Flexural toughness was measured using the area under load–deflection curves (actuator data). Flexural toughness of FRAC-A was 83 times more than AAC at the measured displacement; the projected total toughness is more than 100 times.

3.6. Tensile stress–strain properties

As shown in Fig. 15, direct tensile testing of FRAC was performed on 25 mm × 50 mm × 350 mm (1″ × 2″ × 14″) prisms with an open span of 150 mm (6″) and a circumferential notch of 2 mm (0.08″) at the center of the specimen. Two paralleled LVDTs were used for measuring the axial displacement and the test was performed under closed-loop conditions. The values of the tensile stress–strain, stress–crack-width relationship, strength and tensile toughness were measured using the data for FRAC-A, FRAC-B, and FRAC-C. Three replicate samples were used for each mixture.

The results of the instrumented tensile test for FRAC are presented in Fig. 16 and the experimental parameters are summarized in Table 5. These include tensile strength (F_t), deflection at the maximum load, elastic tensile stiffness (slope of stress–strain

Table 4
Summary of flexural test parameters for AAC and FRAC.

	FRAC-A	FRAC-B	FRAC-C	AAC
MOR: MPa	0.56	0.43	0.27	0.66
Flexural stiffness: N/m	4.35	4.20	4.58	4.06
Toughness at 10.2 mm displ. N m	17.75	15.25	9.19	0.30
Normalized toughness at 10.2 mm displ.: N/m	934	802	483	15
Toughness at 15.2 mm displ. N m	24.27	21.83	13.16	0.30
Normalized toughness at 10.2 mm displ.: N/m	1,277	1,149	692	15
Axial displ. at peak: mm	3.683	2.896	2.921	0.076
CMOD at peak: mm	5.639	4.445	4.546	0.051
Axial displ. capacity: mm	>10	>10	>10	0.254
CMOD capacity: mm	>10	>10	>10	0.381

Note: toughness was measured by calculating the area under the flexural load–displacement curves, therefore, has unit of N m. Normalized flexural toughness was measured by dividing the toughness value by the cross sectional area with a resulting unit of: N/m.

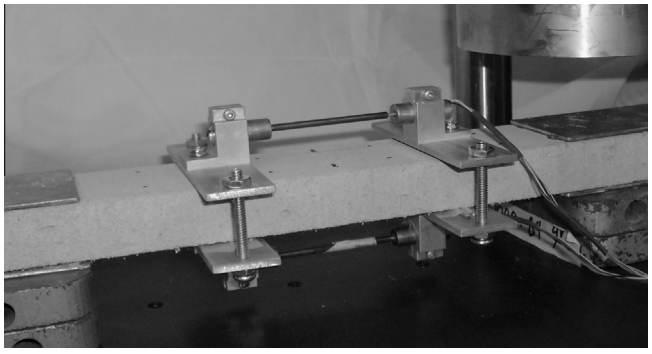

Fig. 15. Instrumented tensile test setup (25 × 50 × 300 mm notched prism).

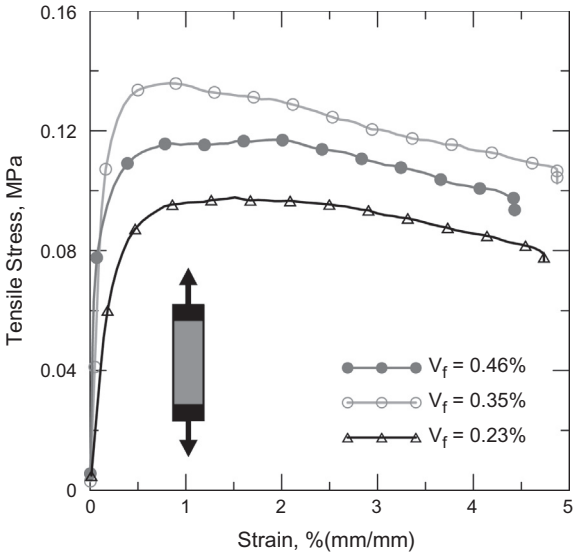

Fig. 16. Tensile strength vs. strain for FRAC material.

curve in the linear portion), and tensile toughness (using the displacement values from actuator). The tensile strength values were in the range of 0.10–0.13 MPa (14–19 psi) with the maximum load occurring in the range of 0.88–1.54 mm (0.035–0.61 in.). The tensile toughness values were measured using the area under load–displacement curves (actuator data) at strain levels of 7.2% and 12.2% and the results are presented in the table. Fig. 17 shows the bridging action of fibers during the tensile loading for FRAC-A which is responsible for the high ductility of aerated fiber reinforced concrete material. The major difference in mechanical

Table 5
Summary of tension test parameters for AAC and FRAC.

	FRAC-A	FRAC-B	FRAC-C
F_t: MPa	0.13	0.12	0.10
Toughness at 7.2% strain level N m	0.720	0.627	0.517
Normalized toughness at 7.2% strain level: N/m	745	649	535
Toughness at 12.2% strain level N m	1.061	0.906	0.728
Normalized toughness at 12.2% strain level: N/m	1,098	937	753
Axial displ. at peak: mm	1.54	0.88	1.38
Axial displ. capacity: mm	>4	>4	>4

Note: toughness was measured by calculating the area under the tensile load–displacement curves, therefore, has unit of N m. Normalized tensile toughness was measured by dividing the toughness value by the cross sectional area with a resulting unit of: N/m.

behavior between AAC and FRAC is the energy absorption capacity or tensile/flexural toughness which is attributed to the bridging action of short fibers.

Having obtained the compressive, tensile, and flexural response for AAC and FRAC materials, one can examine the existing models that relate the mechanical properties from different tests. As described by Soranakom and Mobasher [31], the tensile and compressive mechanical properties can be used to predict the flexural response; also the flexural and compressive responses can be used to predict the tensile behavior of cement-based materials.

3.7. Impact response

As shown in Fig. 18, an instrumented impact test was performed using a hammer drop technique. FRAC-A specimens

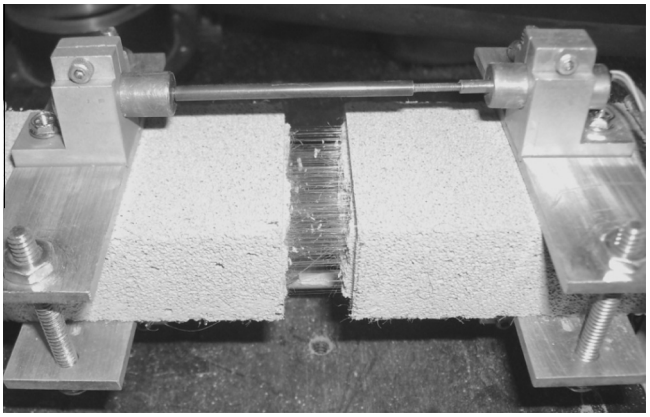

Fig. 17. Crack bridging for notched FRAC-A prism during tensile test.

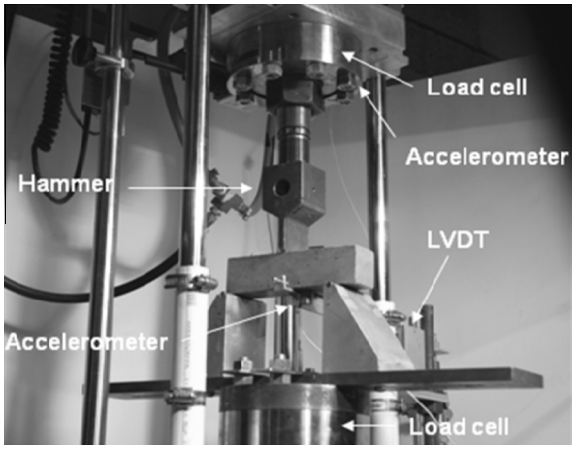

Fig. 18. Instrumented impact test setup (50 × 50 × 250 mm samples).

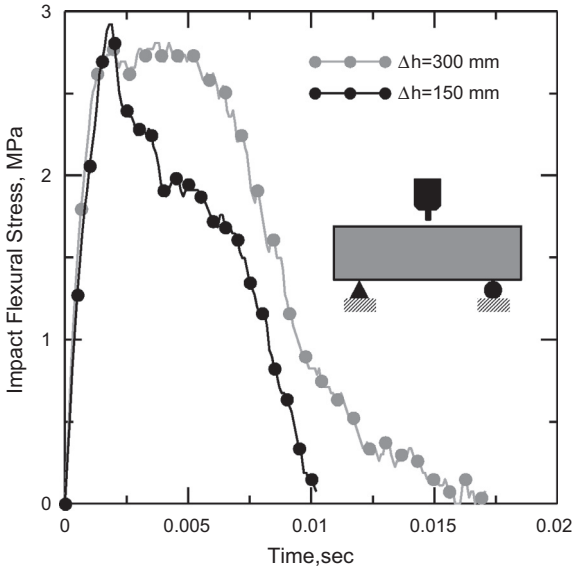

Fig. 19. Impact stress vs. time for FRAC-A at different drop heights.

were used with 50 mm × 50 mm × 250 mm dimensions (200 mm span) on a three-point bending support system. A steel hammer was dropped at two different heights: 150 and 300 mm. The test response was measured using two load-cells and two accelerometers. Three replicate samples were used for the tested mixture (FRAC-A). A MATLAB® code was developed and implemented for filtering the noise occurred during the test and to generate cleaned-up plots for each test. Fig. 19 shows the impact flexural stress against time for FRAC-A tested at various drop heights. The maximum stress is almost the same for the two drop heights; however, the absorbed energy is approximately 50% higher at drop height of 300 mm compared to 150 mm. The corresponding impact velocities were approximately 1300 and 1600 mm/s, respectively. More studies for the impact response of FRAC and AAC are currently being performed.

4. Conclusion

Physical and mechanical properties of Fiber-Reinforced Aerated Concrete (FRAC) were investigated in this work. These properties were also studied for Autoclaved Aerated Concrete (AAC) for comparison. FRAC is a novel lightweight aerated concrete that includes short polymeric fibers without the autoclaving process. Several instrumented experiments were performed to characterize FRAC and AAC blocks. Compression tests showed a pore-crushing mechanism for these aerated products. Compressive strength of AAC was found to be higher than that of FRAC due to different mixture and curing conditions, however, the ratio of residual strength to peak strength for FRAC was much higher than for AAC. While the top portion of a typical FRAC block had higher porosity and less density than the bottom portion due to the non-uniform distribution of air-pores, the residual compressive strength values are more consistent due to the role of fibers in integrating the material after failure. The main difference between the two materials was observed in the flexural and tensile responses. AAC is a brittle material and does not provide much crack resistance under flexural or tensile loading. FRAC on the other hand is a ductile material and absorbs high amounts of energy as a result of crack bridging action of fibers. In comparison, while FRAC had as much as 50% less compressive strength than the studied AAC, its flexural toughness was more than 100 times (for FRAC-A) more than AAC due to the role of fibers in bridging the micro and macro cracks. Fiber-reinforced concrete design guidelines may be used for optimized design of FRAC. Some of these physical and mechanical properties were reported for FRAC-A and published in ICC-ESR-2866 [32]. With very low thermal conductivity values, FRAC can be a used as a sustainable construction material for residential applications.

Acknowledgments

The authors would like to appreciate the financial support of Navajo FlexCrete Inc., as well as the technical support from Babbitt-Nelson Consultants and AAC Structures of Arizona. We also thank Mr. Nathan Zigler, Mr. Derek Morris, and Mr. Geoffrey Minor for their help in sample preparation and testing. We gratefully acknowledge the use of facilities within the Center for Solid State Science at Arizona State University for some of the microstructural studies.

References

[1] Damtoft JS, Lukasik J, Herfort D, Sorrentino D, Gartner EM. Sustainable development and climate change initiatives. Cem Concr Res 2008;38:115–27.
[2] Kuhlmann K, Paschmann H. Beitrag zur Ökologischen Positionierung von Zement und Beton. ZKG Int 1997;50(1):1–8.
[3] ACI 523.2R. Guide for precast cellular concrete floor, roof, and wall units. American Concrete Institute, Farmington Hills, MI; 1996.
[4] Narayanan N, Ramamurthy K. Structure and properties of aerated concrete: a review. Cement Concr Compos 2000;20:321–9.
[5] Mehta PK. High-performance high-volume fly ash concrete for sustainable development. In: Proceedings of the international workshop on sustainable development and concrete technology. Beijing, China; 2004. p. 3–14.
[6] Bentz DP, Hansen AS, Guynn JM. Optimization of cement and fly ash particle sizes to produce sustainable concretes. Cem Concr Compos, doi: 10.1016/j.cemconcomp.2011.04.008.
[7] Sutton ME. Autoclaved Cellular Concrete, the Future of Fly Ash. In: Proceeding of international ash utilization symposium, paper # 73, University of Kentucky, KY; 1999.
[8] Bonakdar A, Mobasher B. Multi-parameter study of external sulfate attack in blended cement materials. J Constr Build Mater 2010;24:61–70.
[9] Bonakdar A, Mobasher B, Dey SK, Roy DM. Correlation of reaction products and expansion potential in ASR for blended cement materials. ACI Mater J 2010;107:380–6.
[10] ASTM C-1693. Standard specification for precast Autoclaved Aerated Concrete (AAC) wall construction units. ASTM International, PA; 2009.
[11] Roels S, Sermijn J, Carmeliet J. Modeling unsaturated moisture transport in autoclaved aerated concrete: a microstructural approach. Building physics 2002 – 6th Nordic symposium, Trondheim, Norway; 2002, p. 167–74.
[12] Nunez E, Nunez SA, Fouad FH. Sustainability in Autoclaved Aerated Concrete (AAC) construction, in Autoclaved aerated concrete, Limbachiya, Roberts, editors. London: Taylor & Francis Group; 2005.
[13] Ng SC, Low KS. Thermal conductivity of newspaper sandwiched aerated lightweight concrete panel. Energy Build 2010;42:2452–6.
[14] Laukaitis A, Fiks B. Acoustical properties of aerated autoclaved concrete. Appl Acoust 2006;67:284–96.

[15] Eden NB, Manthorpe AR, Miell SA, Szymanek PH, Watsont KL. Autoclaved aerated concrete from slate waste – Part 1: Some property/density relationships. Int J Lightweight Concr 1980;2:95–100.
[16] Trunk B, Schober G, Helbling AK, Wittmann FH. Fracture mechanics parameters of autoclaved aerated concrete. Cem Concr Res 1999;29: 855–9.
[17] Perez-Pena M, Mobasher B. Mechanical properties of fiber reinforced lightweight concrete composites. Cem Concr Res 1994;24:1121–32.
[18] Bakhshi M, Mobasher B. Experimental observations of early-age drying of Portland cement paste under low-pressure conditions. Cem Concr Compos 2011;33:474–84.
[19] Gibson LJ, Ashby MF. Cellular solids, structure and properties. Cambridge: Cambridge University Press; 1997.
[20] ASTM C-177. Standard test method for steady-state heat flux measurements and thermal transmission properties by means of the guarded-hot-plate apparatus. ASTM International, PA; 2010.
[21] Othuman MA, Wang YC. Elevated-temperature thermal properties of lightweight foamed concrete. Constr Build Mater 2011;25:705–16.
[22] Mobasher, B., Minor, G., Zenouzi, M., Jalife, S. Thermal and mechanical characterization of contiguous wall systems for energy efficient low cost housing. In: Proceedings of ASME 2011 5th international conference on energy sustainability, August, Washington, DC; 2011.
[23] Khan MI. Factors affecting the thermal properties of concrete and applicability of its prediction models. Build Environ 2002;37:607–14.
[24] Berryman, JG. Thermal conductivity of porous media. Lawrence Livermore National Laboratory, UCRL-JRNL-206118; 2004.
[25] Druma AM, Alam MK, Druma C. Surface area and conductivity of open-cell carbon foams. J Miner Mater Charact Eng 2006;5(1):73–86.
[26] Stang H, Mobasher B, Shah SP. Quantitative damage characterization in polypropylene fiber reinforced concrete. Cem Concr Res 1990;20:540–58.
[27] Hilliard JE, Lawson LR. Stereology and stochastic geometry. Kluwer Academic Publishers; 2003.
[28] Kadashevich I, Schneider HJ, Stoyan D. Statistical modeling of the goemetrical structure of the system of artificial air pores in autoclaved aerated concrete. Cem Concr Res 2005;35:1495–502.
[29] Alexanderson J. Relationship between structure and mechanical properties of autoclaved aerated concrete. Cem Concr Res 1979;9:507–14.
[30] ASTM C-469. Standard test method for static modulus of elasticity and Poisson's ratio of concrete in compression. ASTM International, PA; 2010.
[31] Soranakom C, Mobasher B. Correlation of tensile and flexural responses of strain softening and strain hardening in cement composites. Cem Concr Compos 2008;30:465–77.
[32] ICC-ESR-2866 Evaluation report for Navajo FlexCrete fiber reinforced aerated concrete Masonry blocks; 2011.